Reciprocal excitation of propagating spin waves by a laser pulse and their reciprocal mapping in magnetic metal films

A. Kamimaki,[1,2] S. Iihama,[3] Y. Sasaki,[1,2] Y. Ando,[2] and S. Mizukami[1,*]

[1]*WPI Advanced Institute for Materials Research (AIMR), Tohoku University, 2-1-1, Katahira, Sendai 980-8577, Japan*

[2]*Department of Applied Physics, Graduate School of Engineering, Tohoku University, 6-6-05, Aoba-yama, Sendai 980-8579, Japan*

[3]*National Institute of Advanced Industrial Science and Technology (AIST), Spintronics Research Center, Tsukuba, Ibaraki 305-8568, Japan*

(Received 22 March 2017; revised manuscript received 24 June 2017; published 28 July 2017)

Focused pulse-laser-induced propagating magnetostatic surface spin waves (MSSWs) were investigated using an all-optical space-time-resolved magneto-optical Kerr effect microscope in 20-nm-thick permalloy thin films to clarify reciprocity and symmetry of MSSW emission. The microscope setup was constructed with variable direction of the applied magnetic field, and the corresponding angular dependence was examined. MSSWs were reciprocally emitted from the laser spot, in contrast to the nonreciprocal emission obtained by the antenna method. Specifically, the observed excitation amplitude and phase were independent of the propagation and magnetization directions within experimental error. By transforming the data into wave number–frequency space, the MSSW dispersion relation was clearly identified within the wave number of 2–3 rad/μm and frequency of 10 GHz. These observations are consistent with the model of ultrafast modulation of out-of-plane shape magnetic anisotropy inside the focused laser spot. In addition to confirming the symmetric and reciprocal emission of laser-induced MSSWs, the study demonstrated that this technique can provide all-optical microscopic spectroscopy for MSSW in metals, such as Brillouin light-scattering technique.

DOI: 10.1103/PhysRevB.96.014438

I. INTRODUCTION

Low-energy spin-wave- (or magnon) based devices are attractive possibilities for low-power-consumption magnonic information technologies [1–4]. The spin-wave medium or guides with directionality or nonreciprocity may be important building blocks for magnonic information technology applications [5,6], similar to that for optical information processing applications, and nonreciprocal excitation and detection were also of interest for magnonic devices [4,7–9]. The various characterization techniques for propagating spin waves are important issues in the development of various spin-wave applications and devices. To date, both all-electrical methods and electro-optic hybrid methods have been used to observe and characterize propagating spin waves. Even though the excitation and detection method of spin waves utilizing an antenna is classic, this method is very simple and widely used for investigating spin waves with a nanolithography technique [9–14]. Furthermore, in the hybrid methods, spin waves are exited electrically by the antenna, quantum-mechanical current-induced torque, or pure spin current, and then the exited spin wave is detected with high spatial resolution by the scanning magneto-optical Kerr effect (MOKE) [15–17], by x-ray magnetic circular dichroism [18], and by Brillouin light scattering (BLS) using a focused laser [19–21]. In particular, microfocused BLS is a powerful table-top tool for observing low-energy spin waves in space and time resolution, and a phase-sensitive method has also been developed [22,23].

The all-optical femtosecond pump-probe time-resolved MOKE is also a powerful tool for investigating very fast spin dynamics in the time domain with subpicosecond time resolution and a broad band up to the terahertz range. By applying this method to metallic magnets, so-called ultrafast demagnetization has been unveiled [24], in which a femtosecond laser pulse excitation changes the degree of magnetic order in the subpicosecond time scale. Various ultrafast phenomena accompanying ultrafast demagnetization, such as superdiffusion spin current, have also been discussed [25]. Laser pulse irradiation under a magnetic field can also yield coherent magnetization precession via an ultrafast change in the magnetic anisotropy, known as all-optical ferromagnetic resonance (FMR) [26]. In this process, the pump-induced magnetization precession inside the pump spot can be detected by a probe beam at the same position, enabling the local detection of spin dynamics for various magnetic materials up to the terahertz wave range [27–30].

Such all-optical pump-probe methods have also been applied in the detection of propagating magnetostatic spin waves (MSWs). When the pump spot size becomes comparable to or smaller than the length scale for the group velocity of a MSW divided by the FMR mode frequency, the precession of the magnetization propagates as a MSW from the pump spot area. In this case, the pump beam spot behaves as a MSW source, which has been demonstrated by an insulating ferrimagnetic garnet of $Gd_{4/3}Yb_{2/3}BiFe_5O_{12}$ [31]. MSWs in such ferrimagnets have a long lifetime, propagating over hundreds of micrometers. Moreover, such ferrimagnets show transparency to light with the proper wavelength of laser pulses even though its thickness is the order of micrometers. Although such experiments are more difficult in metallic films than in such insulators since a relatively large Gilbert damping in metals, propagating MSWs induced in metals have been observed using a laser pulse under a microscope [32–34]. Au *et al.* first reported the excitation of the propagating MSW by a laser pulse in metals and discussed the mechanism. Their micromagnetic simulation based on the Landau-Lifshitz-Baryakhtar equation showed neither symmetric nor antisymmetric MSW emission pattern relative to the direction of the in-plane projection of the bias

*shigemi.mizukami.a7@tohoku.ac.jp

magnetic field [32]. Au *et al.* interpreted that the symmetric pattern caused by the transient out-of-plane demagnetizing field and the torque induced by a symmetric transient in-plane demagnetizing field were actually antisymmetric, which resulted in an antisymmetric MSW emission pattern. The presence of both mechanisms produced the mixed pattern [32]. In our previous communication, we reported that the MSW emission could be well described by the excitation due to out-of-plane magnetic field induced in the laser spot, i.e., a symmetric excitation. However, the observed MSW was slightly asymmetric in amplitude, which remained as one of the issues [34]. Thus, neither experimental evidence nor a detailed discussion of reciprocity and symmetry was reported, unlike nonreciprocity in the case of MSW excited by electrical means [4,7–9,17].

In this article, we study propagating magnetostatic surface spin-waves (MSSWs) exited by a laser pulse in detail to examine the reciprocity and symmetry of laser-induced MSSWs in metals. By constructing the microscopy setup with a variable direction of the applied magnetic field, we confirmed the reciprocity and symmetry of MSSWs in both real space-time and wave-number–frequency spaces with different magnetic field direction, consistent with the consideration that the ultrafast modulation of out-of-plane shape magnetic anisotropy within the pump laser spot is the dominant driving source of MSSWs. In addition, the study demonstrated that this technique could be a tool for visualizing the dispersion relation of MSSW in metals.

II. EXPERIMENTAL METHODS

The measurements in this study were performed with standard-pump-probe optics, as previously described [34]. A Ti:sapphire laser with a wavelength, pulse width, and pulse repetition rate of $\simeq$800 nm, $\simeq$120 fs, and $\simeq$80 MHz, respectively, was used for the light source of the probe beam. The frequency of the pump laser pulse was doubled by a BaB_2O_4 (BBO) crystal, so that the wavelength of the pump beam is $\simeq$400 nm, and its amplitude was modulated by a mechanical chopper with a modulation frequency of 370 Hz. Both the probe and pump pulse laser beams were focused on a film sample via an objective lens ($\times$50, N.A. = 0.65), as schematically shown in Fig. 1. Here the probe spot position was variable using an electrically controlled mirror, while the position of the pump laser spot was fixed. The spot radius σ, i.e., the half-width at which the light intensity becomes $1/\sqrt{e}$, for both the pump and probe beams was about 0.5 μm, where the pump beam was slightly defocused [34]. The optical paths were carefully optimized in such a way that both spots become circular and that were monitored using a charge-coupled device camera. The fluence of the pump laser pulse on the film surface was below 1.1 mJ/cm^2, which was much larger than that for the probe pulse. The sample film was a trilayer Ta(5 nm)/$Ni_{80}Fe_{20}$(20 nm)/Ta(5 nm) film deposited onto a thermally oxidized Si substrate using magnetron sputtering. The pump laser-induced change in the polar Kerr rotation angle of the probe laser pulse, $\Delta\theta_K$, was detected by a Wollaston prism and a balanced photodiode detector with a lock-in amplifier. An electromagnet was specially designed for this study, and the setup was constructed in a such a manner that the sample

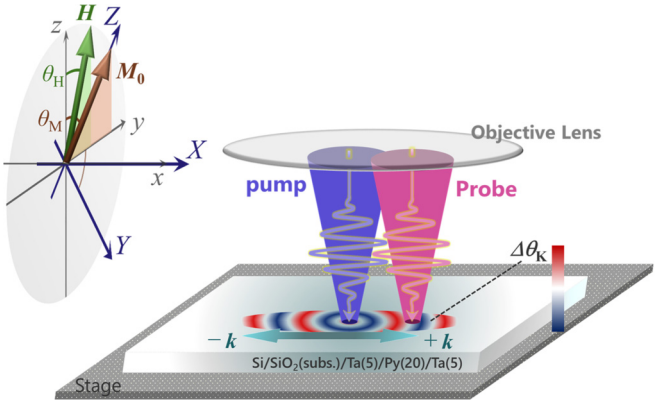

FIG. 1. Schematic illustration of the coordinate system in this experiment. Both the applied magnetic field **H** and macroscopic magnetization vector $\mathbf{M}_0$ lie in the y-z plane. The polar angle of **H** and $\mathbf{M}_0$ are denoted as θ_H and θ_M, respectively. The probe laser spot is scanned along the x axis with the origin being defined as the center of the pump laser spot. The X-Y-Z coordinate system is defined as $Z \parallel \mathbf{M}_0$ and $X \parallel x$.

was placed on the sample stage with an applied magnetic field $\mu_0 H$ of 0.3 T, whose angle θ_H could be changed with respect to the film normal (Fig. 1) [35]. Here μ_0 is the permeability of vacuum.

The magnetic field angle θ_H is a very important factor for the observation of MSWs in metals in this all-optical method. If we regard the transient out-of-plane demagnetization as the dominant source of MSW excitation, then there would be negligible MSW excitation in the in-plane configuration, i.e., $\theta_H = 90^\circ$ and the magnetic field would be sufficiently large to saturate magnetization, as the excitation torque would be negligibly small. Similarly, when magnetization was saturated with the applied magnetic field at $\theta_H = 0^\circ$, both the excitation torque and the dynamic magnetization would be negligibly small. Thus we selected intermediate values for θ_H, $\pm 4^\circ$ and $\pm 14^\circ$ for the measurements such that the observed amplitude would be sufficiently large. In this case, the magnetization direction was still nearly parallel to the film plane due to the small magnetic field, as described later. This geometry was different from that in a conventional MSW propagation experiment using microwave excitation, where the applied magnetic field is parallel to the film normal or parallel to a film plane, since both the experimental and theoretical description in the conventional experiment are much simpler.

III. EXPERIMENTAL RESULTS AND DISCUSSIONS

Figure 2 shows $\Delta\theta_K$ measured at the magnetic field angle θ_H of -4° as a function of x with different pump-probe delay times Δt. Here x is defined as the position for the center of the probe beam spot along the x axis with respect to origin, which is the center of the pump beam spot (Fig. 1). Moreover, $\Delta\theta_K$ is proportional to the normal component of the pump-induced change of magnetization, averaged inside the probe beam spot, so that the large peak in $\Delta\theta_K$ about the origin results from the ultrafast reduction of magnetization due to the pump pulse irradiation [Fig. 2(a)]. Subsequently, two small peaks of $\Delta\theta_K$ are observed near the origin [Fig. 2(b)], and these small peaks

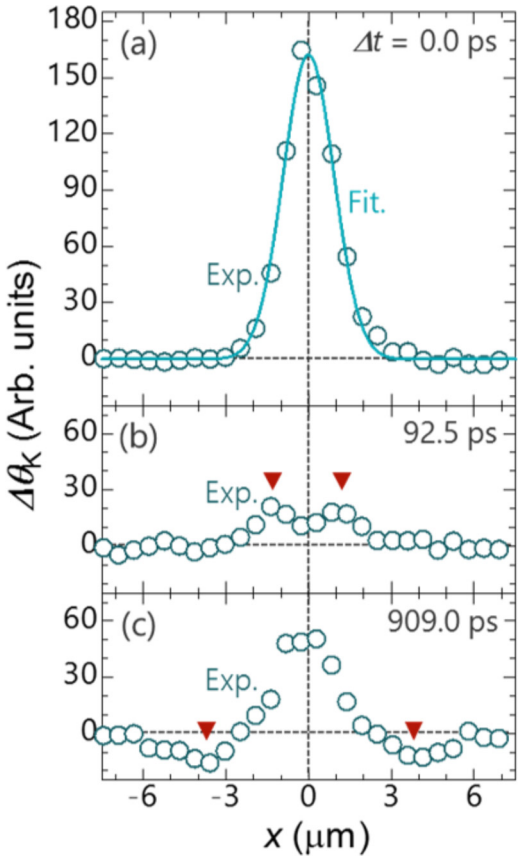

FIG. 2. The pump-laser-induced change in the Kerr rotation angle $\Delta\theta_K$ measured at a θ_H of -4° as a function of the position x for the pump-probe delay time Δt of (a) 0.0, (b) 92.5, and (c) 909.0 ps. The curve is a Gaussian function fitted to the data, and the arrows indicate the spin-wave emission.

move away from the origin as a wave packet, as shown in Fig. 2(c). The spatiotemporal change of the small peaks in $\Delta\theta_K$ corresponds to propagation of the MSSW packets emitted from the demagnetization area.

The magnitude of $\Delta\theta_K$ stemming from MSSW is much smaller than that due to the demagnetization. To more clearly visualize $\Delta\theta_K$ stemming from MSSW, we approximately separate it from $\Delta\theta_K$ by assuming the following relation:

$$\Delta\theta_K(x,\Delta t) \simeq \Delta\theta_K^{\mathrm{mag}}(x,\Delta t) + \Delta\theta_K^{\mathrm{sw}}(x,\Delta t), \qquad (1)$$

where the first and second terms on the right-hand side of the equation represent $\Delta\theta_K$ due to demagnetization and MSSW, respectively. In general, $\Delta\theta_K^{\mathrm{mag}}$ is caused by the ultrafast demagnetization and the following gradual temporal change of magnetization due to heat dissipation; $\Delta\theta_K^{\mathrm{mag}}$ may also show nonoscillatory changes in space and time similar to the conventional all-optical FMR [27–30]. Thus, $\Delta\theta_K^{\mathrm{mag}}$ was subtracted from the original data of $\Delta\theta_K$ with respect to Δt collected at each x using the following relation:

$$\Delta\theta_K^{\mathrm{mag}} = A + B\exp\left(-\frac{\Delta t}{\tau}\right).$$

Here A, B, and the relaxation time τ are constants determined by the fitting. A and B showed a Gaussian distribution with respect to x and τ were independent of x within acceptable levels of error (see more details in Appendix B). Figures 3(a) and 3(b) showed $\Delta\theta_K^{\mathrm{sw}}$ as a function of Δt and x measured at $\theta_H = 4^\circ$ and -14°, respectively. The strip-like patterns symmetrically extend away from the origin, corresponding to spatiotemporal evolutions of MSSW, and the slope denoted by the arrows is the motion of the wave-packet center of mass. The strip pattern observed at $\theta_H = 4^\circ$ spread more than that observed at $\theta_H = -14^\circ$, indicating that the group velocity v_g of the MSSW-packet decreases with increasing θ_H. In Figs. 3(c)–3(f), the wave packet form measured with different field angles θ_H and positions x are shown as a function of time Δt. The wave packets propagating in the positive direction completely overlap with those propagating in the negative direction, confirming reciprocal excitation and propagation within experimental errors.

As performed in the previous study, we first analyzed the time-domain data at each position x using a sinusoidal wave function with a Gaussian envelope:

$$\Delta\theta_K^{\mathrm{sw}}(x,\Delta t) \sim A_{\mathrm{sw}}\exp\left[-\frac{(\Delta t - t_0)^2}{2\sigma_t^2}\right]\sin(2\pi f_0\Delta t - \phi), \qquad (2)$$

where A_{sw}, σ_t, and t_0 are the amplitude, width, and center of the Gaussian envelope of $\Delta\theta_K^{\mathrm{sw}}$, respectively. Besides, f_0 and ϕ represent the frequency and phase of the sinusoidal wave part of $\Delta\theta_K^{\mathrm{sw}}$, respectively. The typical fitting results are shown in Figs. 3(c)–3(f) with solid curves. The experimental data at $x = \pm 2.1$ μm for $\theta_H = 4^\circ$ slightly deviated from that in the fitted curve in $\Delta t > 1000$ ps. In contrast, the experimental data for $\theta_H = -14^\circ$ was well fitted to the curve calculated by Eq. (2). This difference may be caused by the difference in the dispersion relation depending on the field angle. Figure 4 displays the typical physical quantities, i.e., the mean value of the wave number k_0, f_0, and v_g for the excited MSSWs obtained from the fitting. Here k_0 and v_g were experimentally evaluated with the relation:

$$\phi = k_0 x + \phi_0,$$
$$t_0 = x/v_g,$$

from the data of ϕ vs. x and t_0 vs. x, respectively, where ϕ_0 is the initial phase at $x = 0$ μm. Theses quantities were independent of the MSSWs propagation direction and showed symmetric changes against the field angle θ_H with respect to the film normal within experimental error, as shown in Fig. 4. The value for k_0 was 0.87 rad/μm on average [Fig. 4(a)]. The experimental values for f_0 and v_g show systematic changes against θ_H, as shown in Figs. 4(b) and 4(c), respectively. The theoretical values for f_0 were calculated using the following equation of dispersion relation of MSSWs with the arbitrary angle of magnetic field [36]:

$$f(k_x, k_y = 0) = \mu_0\frac{\gamma}{2\pi}\sqrt{H_{XX}H_{YY}}, \qquad (3)$$

with

$$H_{XX} = H_{XX0} + M_S\eta(k_x) + \frac{2A}{\mu_0 M_S}k_x^2,$$
$$H_{YY} = H_{YY0} - M_S\eta(k_x)\sin^2\theta_M + \frac{2A}{\mu_0 M_S}k_x^2,$$

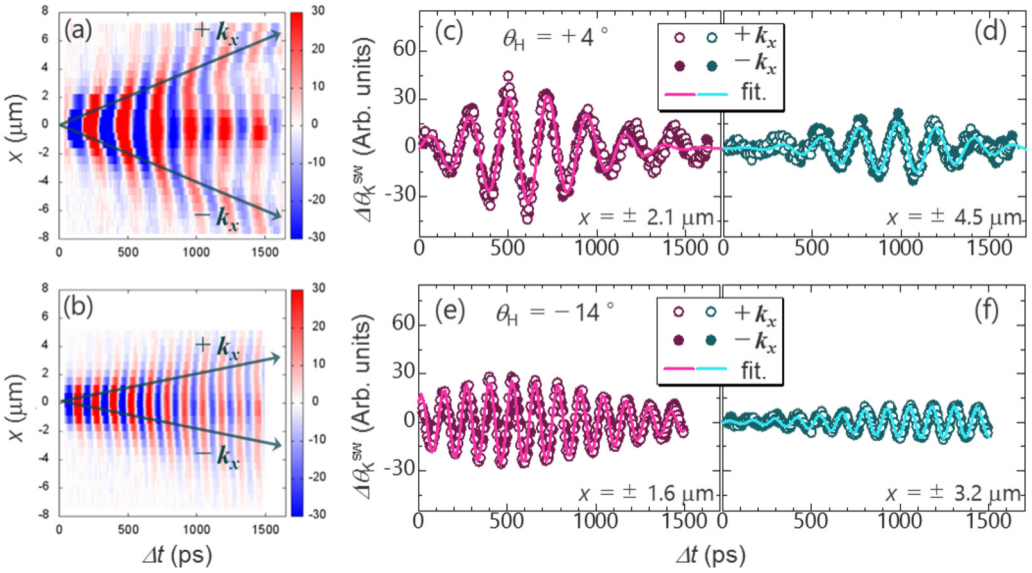

FIG. 3. Space-time mapping of the pump-laser-induced change in the Kerr rotation angle due to the MSSW for $\Delta\theta_K^{\rm sw}$ obtained at θ_H of (a) 4° and (b) -14°. The arrows are a visual guide showing the spatiotemporal evolution of the MSSWs. The time dependence of $\Delta\theta_K^{\rm sw}$ at θ_H of 4° obtained at (c) $x = \pm 2.1$ μm and (d) $x = \pm 4.5$ μm. Similar data at θ_H of -14° obtained at (e) $x = \pm 1.6$ μm and (d) $x = \pm 3.2$ μm. Open (solid) circles represent the data recorded at $x > 0$ μm ($x < 0$ μm). Solid curves in (c), (d), (e), and (f) are the calculated data fitted to the experimental ones.

$$H_{XX0} = H\cos(\theta_H - \theta_M) + H_k^{\rm eff}\cos^2\theta_M,$$
$$H_{YY0} = H\cos(\theta_H - \theta_M) + H_k^{\rm eff}\cos 2\theta_M,$$

where the wave-number-dependent factor $\eta(k_x)$ can be expressed as

$$\eta(k_x) = 1 - \frac{1 - e^{-k_x d}}{k_x d},$$

and the magnetization angle θ_M was computed by the balance equation:

$$H\sin(\theta_H - \theta_M) - H_k^{\rm eff}\sin\theta_M\cos\theta_M = 0. \quad (4)$$

Moreover, the theoretical values for v_g was also obtained with the relation:

$$v_g = 2\pi\frac{df}{dk_x}.$$

The following experimentally obtained values were used for the calculations of f_0 and v_g: gyromagnetic ratio $\gamma/2\pi = 29.7$ GHz/T, saturation magnetization $M_S = 750$ kA/m, effective out-of-plane magnetic anisotropy $H_k^{\rm eff} = -M_S$, thickness $d = 20$ nm, exchange stiffness $A = 14$ pJ/m, and $k_x = k_0$. The calculated data of f_0 and v_g are shown in Figs. 4(b) and 4(c) with solid curves, respectively. Both calculated data agree well with the experimental data, indicating that the propagation of MSSWs observed is close to one-dimensional propagation. In this case, $\theta_M = \pm 72^\circ$ and $\pm 73^\circ$ were evaluated for $\theta_H = \pm 4^\circ$ and $\pm 14^\circ$ using Eq. (4), respectively; thus, the geometry was approximately an in-plane configuration.

When the X-Y-Z coordinate is taken as shown in Fig. 1, the observed MSSWs represent the spatiotemporal dynamics of the z-projected transverse magnetization $\tilde{m}_Y$. This relationship can be theoretically expressed as the nonlocal space $\mathbf{r} = (x, y)$ and time t relationship with a transverse effective magnetic field induced by a pump laser pulse $\tilde{h}_{X,Y}$ under a linear response regime with a thin-film approximation of the magnetostatic field:

$$\tilde{m}_Y(\mathbf{r},t) = \sum_{j=X,Y}\iiint d^2r'dt' \times\tilde{\chi}_{Yj}(\mathbf{r}-\mathbf{r}',t-t')\tilde{h}_j(\mathbf{r}',t'). \quad (5)$$

Here the kernel $\tilde{\chi}_{Yj}$ is the magnetic susceptibility tensor. The Fourier transform of Eq. (5) yields $\tilde{m}_Y$ in the wave number $\mathbf{k}$ and frequency ω space:

$$\tilde{m}_Y(\mathbf{k},\omega) = \sum_{j=X,Y}\tilde{\chi}_{Yj}(\mathbf{k},\omega)\tilde{h}_j(\mathbf{k},\omega). \quad (6)$$

Therefore, $\Delta\theta_K^{\rm sw}$ in $\mathbf{k}$ and ω space may more directly provide information on the amplitude and phase of the excited MSSW modes and excitation fields. Here $\Delta\theta_K^{\rm sw}$ is shown as a function of k_x and f ($\equiv \omega/2\pi$) with different θ_H obtained by the fast Fourier transform (FFT) in Fig. 5. Some curved structures are observed in the both real and imaginary parts of the FFT spectrum for $\Delta\theta_K^{\rm sw}$. The theoretical curves for the dispersion relations shown in Figs. 5(a)–5(d) are similar to the structures observed in the FFT data. The slight difference between the experimental and theoretical data may come from the possible calibration uncertainties in θ_H and H. The real part of the FFT data shows the maximum values along the curves of the dispersion relation. On the other hand, the sign of the FFT intensity changes along the curves of the dispersion relation in the corresponding imaginary parts of the data. In addition, the dispersion relations are visible only within $|k_x|$ of 2–3 rad/μm. These features may be related to the spatial dependence of and the relative magnitude of $\tilde{h}_X$ and $\tilde{h}_Y$ in Eq. (6). As mentioned in Sec. I, Au *et al.* discussed two types of excitation fields induced by ultrafast demagnetization that could be attributed

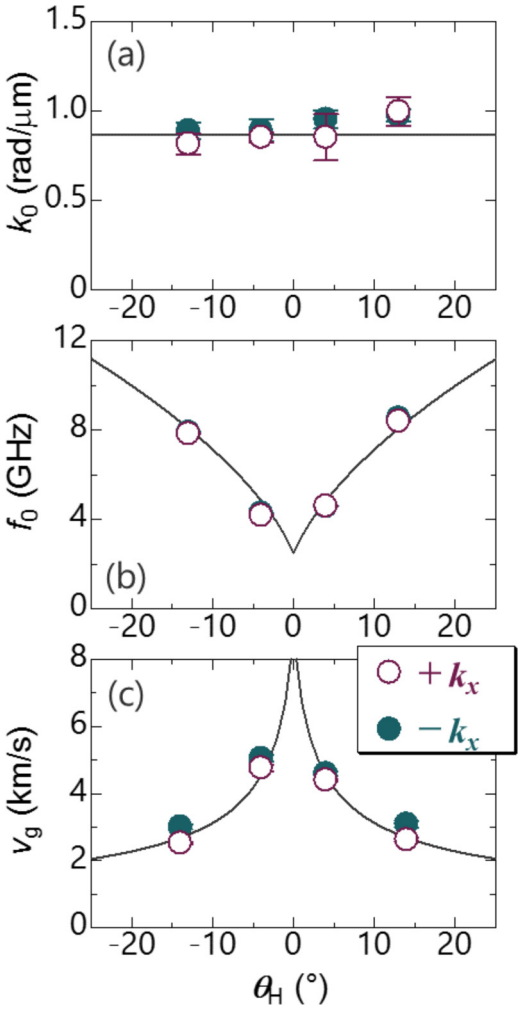

FIG. 4. Field angle dependence of (a) the average wave number k_0, (b) the frequency f_0 for the sinusoidal change in the MSSW packet, and (c) the group velocity v_g with different propagation directions. Solid line in (a) is a visual guide, and solid curves in (b) and (c) are the calculated data.

to the transient out-of-plane and in-plane demagnetizing field, which caused different spin-wave emission patterns, i.e., symmetric and antisymmetric, respectively [32]. In the X-Y-Z coordinate, the transient out-of-plane demagnetizing field dominantly causes $\tilde{h}_Y$. On the other hand, the transient in-plane demagnetizing field causes both $\tilde{h}_X$ and $\tilde{h}_Y$. The data in Fig. 5 showed symmetric patterns similar to the dispersion structure; therefore the contribution of $\tilde{h}_X$ could be disregarded for the discussion in this study. When we assume $\tilde{h}_X$ is negligible and $\tilde{h}_Y$ is a result of the change in the out-of-plane shape magnetic anisotropy field induced by ultrafast demagnetization in the pump spot area, the theory suggests the following proportionality (see Appendix A):

$$\Delta\theta_K^{\rm sw}(k_x,\omega) \propto i\,\tilde{\chi}_{YY}(k_x,k_y=0,\omega)G_{\rm mp}(k_x). \tag{7}$$

Here $G_{\rm mp}(k_x)$ is the Fourier transform of the Gaussian function $G_{\rm mp}(x)$ corresponding to the demagnetization area:

$$G_{\rm mp}(k_x) = \sqrt{2\pi}\sigma_{\rm mp}\exp\left(-\tfrac{1}{2}\sigma_{\rm mp}^2 k_x^2\right).$$

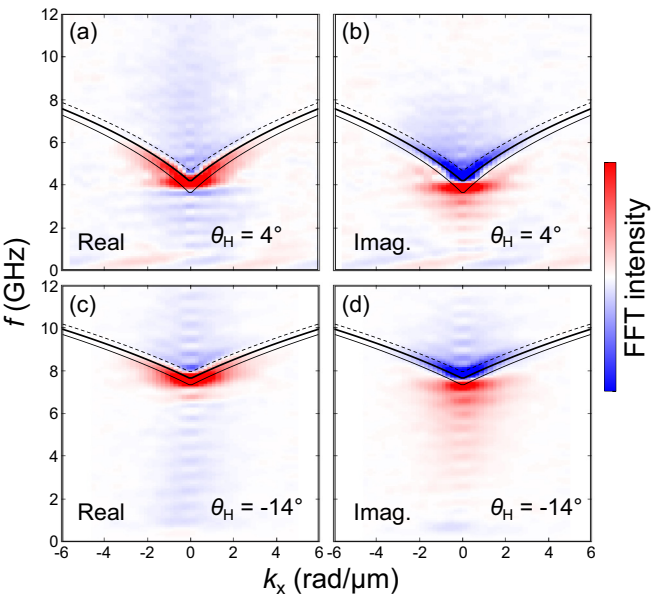

FIG. 5. The frequency f and wave number k_x map of the spectrum density for the pump-laser-induced change in the Kerr rotation angle due to the MSSW, $\Delta\theta_K^{\rm sw}$; (a) the real part and (b) the imaginary part at $\theta_H = 4°$, and (c) the real part and (d) the imaginary part at $\theta_H = -14°$. The thin, thick, and dashed curves in (a) and (b) [(c) and (d)] are the calculated data of the dispersion relation of MSSW for different magnetic field angles of 3°, 4°, and 5° (−12°, −13°, and −14°), respectively.

Moreover, $\sigma_{\rm mp}$ is the mean square of the Gaussian width for the demagnetization area σ_m and for the probe beam spot σ_p, i.e.,

$$\sigma_{\rm mp} \equiv \sqrt{\sigma_m^2 + \sigma_p^2}.$$

Here the probe beam spot used in the equation comes from the fact that the observed data is the average of the probe beam weighted by the Gaussian distribution. Finally, $\tilde{\chi}_{YY}(\mathbf{k},\omega)$ can be approximately described with the spin-wave mode frequency $\omega_{\mathbf{k}}$ and lifetime $\tau_{\mathbf{k}}$:

$$\tilde{\chi}_{YY}(\mathbf{k},\omega) \simeq \frac{\omega_M}{\omega - \omega_{\mathbf{k}} + i/\tau_{\mathbf{k}}}. \tag{8}$$

Here $\omega_M \equiv \mu_0\gamma M_S$. Equations (7) and (8) indicate that the real (imaginary) part of the FFT data is proportional to the imaginary (real) part of $\tilde{\chi}_{YY}(k_x,k_y=0,\omega)$, i.e., the Lorentzian absorption (dispersion) curves with respect to ω at each k_x. Moreover, the FFT data should have large values in $|k_x| < \sqrt{2}\sigma_{\rm mp}^{-1}$ due to the Gaussian function $G_{\rm mp}(k_x)$. The value for $\sigma_{\rm mp}$ of 0.8 μm was estimated from the Gaussian fitting shown in Fig. 2(a), corresponding to $\sqrt{2}\sigma_{\rm mp}^{-1} = 1.8$ rad/μm; thus, the above consideration is consistent with the experimental observation. To further examine this consideration, the FFT data were also obtained from the data of the theoretical $\Delta\theta_K^{\rm sw}$ calculated using the same parameters as those in Fig. 5 [34]. The theoretical FFT data are shown in Fig. 6. The above-mentioned features in Fig. 5 were also seen in Fig. 6, except for the data at $f \simeq 0$. This slight difference at $f \simeq 0$ may stem from the approximation of the disentanglement between $\Delta\theta_K^{\rm mag}$ and $\Delta\theta_K^{\rm sw}$ in the experiments [Eq. (1)].

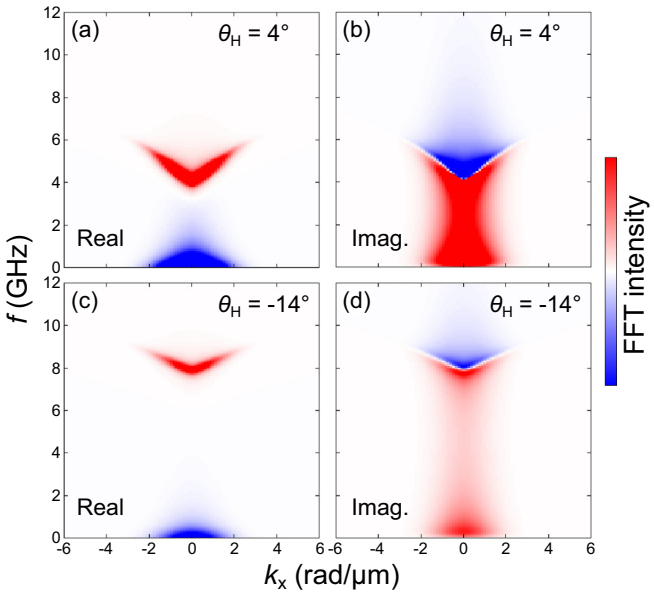

FIG. 6. The theoretical frequency f and wave number k_x map of the spectrum density for the pump-laser-induced change in the Kerr rotation angle due to the MSSW, $\Delta\theta_K^{\rm sw}$; (a) the real part and (b) the imaginary part at $\theta_H = 4^\circ$, and (c) the real part and (d) the imaginary part at $\theta_H = -14^\circ$.

In Fig. 5, the observed shape of the dispersion relations and the strength of the real and imaginary parts are symmetric with respect to the sign of k_x, which also indicates reciprocity, as shown in the real space and time data (Figs. 3 and 4). Frequency nonreciprocity in the MSSW dispersion has been recently discussed in terms of the chiral asymmetry caused by the interfacial Dzyaloshinskii-Moriya interaction (DMI) and/or the asymmetric interface magnetic anisotropy for the top and bottom interfaces [37–42]. The interfacial DMI works in thin bilayer films composed of magnetic metal and heavy metal and its strength becomes larger as the magnetic layer thickness decreases, typically less than 10 nm. The sample studied here is relatively thicker and has a roughly symmetric stacking structure even though the heavy element Ta layer was used. Therefore, the DMI effect on the frequency nonreciprocity may be negligible in our films, which is consistent with the experiments. On the other hand, the nonfrequency reciprocity for MSSW due to the asymmetric interface magnetic anisotropy tends to be enhanced with increasing magnetic layer thickness and also observed even in films with symmetric stacking films. For instance, the difference in f for $\pm k_x$ for Al_2O_3/permalloy(20 nm)/Al_2O_3 films evaluated by the electrical antenna method was observed to be about 50 MHz, this may be due to slight difference in atomic structure between the bottom and top interface [42]. Although this asymmetric anisotropy effect could also work on the film in this study, this effect may be smaller than the frequency resolution, $\simeq$0.2 GHz, in the present experiment.

Finally, we comment on the difference between BLS and the technique described here, both of which can be used to obtain information on the MSSW dispersion relation in purely optical methods. The conventional BLS technique detects spin waves by the inelastic scattering of light. The ω and $\mathbf{k}$ values for spin waves are determined by the frequency shift for the scattered light with respect to the incident light and by scanning the incidence angle of light in the case of a backscattering geometry, respectively [43]. Consequently, an objective lens must have a sufficiently large working distance in order to have space enough to change the incident angle, making the measurement in micron-sized areas difficult. On the other hand, the microfocused BLS cannot easily observe spin waves with different wave vectors as the incident angle of light is not sufficiently well defined to achieve high spatial resolution with the objective lens [43]. Instead of a purely optical method, the phase-sensitive technique for the microfocused BLS was used for characterizing a spin-wave, and its dispersion can also be obtained by the spatial resolution with the electrical excitation of a coherent spin-wave [23,43]. Even though the resolution in the wave-number space was not high, this technique was developed for probing standing spin-wave modes localized on ferromagnetic nanostructures and all relevant information can be obtained in the spatiofrequency mapping.

In the present measurement, discrete wave vectors cannot be fixed, but we can obtain the spectrum in a small physical area with an all-optical method, which is different from the microfocused BLS technique. The range of $|k_x|$ for visualizing the dispersion relation can be increased according to the above discussion for Eq. (7), i.e., $|k_x| < \sqrt{2}\sigma_{\rm mp}^{-1}$. Figure 7 displays the theoretical f–k_x map at $\theta_H = 4^\circ$ simulated using the same parameters as those for the present sample with different sizes for σ_m and σ_p. The pattern of the data in Fig. 7 are essentially the same as those discussed in Fig. 5, whereas the visualized range of dispersion relation expands with decreasing σ_m and σ_p. By reducing the spot size for both the pump and probe beams to approximately half of light wavelength $\lambda/2$ in the diffraction limit, e.g., $|k_x| \simeq 10$ rad/μm is achieved at σ_m and σ_p of $\simeq$100 nm at $\lambda \simeq 400$ nm. This $|k_x|$ value is by a factor of approximately 2 smaller than the maximum detectable value of the wave number using the recent non-micro-focused BLS techniques due to the backscattering geometry [37,39,40]. Thus this all-optical method is not superior to the conventional BLS concerning the maximum wave number for MSSWs.

The all-optical technique studied here might be used for investigating MSSW with interfacial DMI in micron-sized structures and for electrical tuning of the propagation of MSSW in a micron-sized capacitive structure [35,44,45]. However, such systems usually require very thin magnetic layers of less than 5 nm in thickness and a heavy metal capping or buffer layer with a high spin-orbit coupling, in which the group velocity and propagation length of MSSW become much smaller than those in this study. Therefore, it will be a physically interesting and challenging issue to observe MSSWs in such systems using this microscopic all-optical method.

IV. SUMMARY

Focused pulse-laser-induced propagating MSSWs were investigated using the all-optical space-time-resolved MOKE microscope in the 20-nm-thick permalloy thin films. The experimental setup was constructed with variable direction of the applied magnetic field, and the angular dependence was also examined. The excitation amplitude and phase for MSSW were

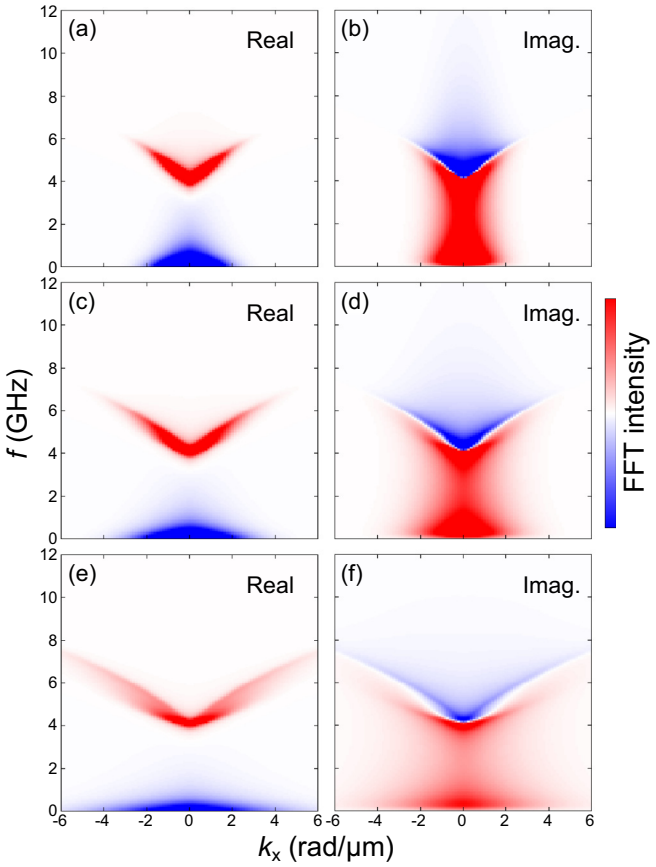

FIG. 7. The theoretical frequency f and wave number k_x map of the spectrum density for the pump-laser-induced change in the Kerr rotation angle due to the MSSW, $\Delta\theta_K^{\rm sw}$. The data computed at $\theta_H = 4^\circ$ with the different size of the demagnetization area σ_m and probe beam σ_p. Panels (a), (c), and (e) [panels (b), (d), and (f)] are the real part (the imaginary part) of the data for the case of $\sigma_m = \sigma_p =$ 500, 300, and 150 nm, respectively.

independent of the propagation and magnetization direction within experimental error. The MSSW dispersion relation was experimentally visualized in the wave number and frequency space within the wave number of 2–3 rad/μm, which was in accordance with the theoretical dispersion relation of MSSW. The data observed in the Fourier space were well explained with the theory considering the ultrafast change in out-of-plane shape magnetic anisotropy inside the pump laser spot. Thus, we confirmed the reciprocal and symmetrical MSSW emission induced by the laser pulse. The study also demonstrated that the dispersion relation of MSSW for micron-sized areas of metallic magnets can be gained using the proposed all-optical method.

ACKNOWLEDGMENTS

We thank A. Sakuma for fruitful discussions. This work was partially supported by Grants-in-Aid for Scientific Research (No. 26103004 and No. 16H03846), the Center for Spintronics Research Network (CSRN), and the JSPS Core-to-Core Program. A. K. and Y. S. thank the Graduate Program of Spintronics in Tohoku University, and S. I. thanks the Grant-in-Aid for JSPS Fellows (No. 28-7881).

APPENDIX A: THEORETICAL BACKGROUND

1. Magneto-optical Kerr effect using focused pump and probe laser pulses

Here we introduce the mathematical treatment of the magneto-optical Kerr effect using focused pump and probe laser pulses. The magnetization vector $\mathbf{M}_0$ is oriented in the direction with angle θ_M determined by the balance between the Zeeman energy due to the magnetic field vector $\mathbf{H}$ and the out-of-plane magnetic anisotropy, which mostly originates from the out-of-plane shape magnetic anisotropy in this sample. For simplicity, we neglect any changes of the physical quantities along the depth direction, even though the light penetration depth for the present sample is less than the thickness [46]. This assumption may be a good approximation for the observed dynamics, because the depth-dependent dynamics, such as the standing spin-wave mode, were not observed in this study. Thus, the problem is entirely two dimensional in space.

The pump-laser-induced change of the magnetization $\mathbf{M}$ is expressed as

$$\Delta\mathbf{M}(\mathbf{r},t) = \mathbf{M}(\mathbf{r},t) - \mathbf{M}_0.$$

The polar MOKE was considered in this setup. When we neglect the change in the optical constant due to heating of the pump laser pulse, the pump-induced change of the polar Kerr rotation angle $\Delta\theta_K$ is proportional to the normal component of the pump-induced change of magnetization ΔM_z averaged inside the probe beam spot on the film surface:

$$\Delta\theta_K(\mathbf{r},t) = \frac{\theta_{K,S}}{M_S}\iint \Delta M_z(\mathbf{r}-\mathbf{r}',t)g_p(\mathbf{r}')d^2r', \qquad \text{(A1)}$$

where M_S is the saturation magnetization at pump-off, and $\theta_{K,S}$ is the corresponding polar Kerr rotation angle at saturation. Here $\mathbf{r}$ is a two-dimensional position vector, namely $\mathbf{r} = (x,y)$, and the x-y-z coordinate is taken as shown in Fig. 1 in the main text. The Gaussian distribution function $g_p(\mathbf{r})$ of the laser intensity for the probe beam is given as

$$g_p(\mathbf{r}) = \frac{1}{2\pi\sigma_p^2}\exp\left(-\frac{r^2}{2\sigma_p^2}\right), \qquad \text{(A2)}$$

with width σ_p. Note that the duration of the probe laser pulse was neglected in Eq. (A1) because the ultrafast process comparable to the pulse duration is not treated here.

Under a weak pump fluence limit, $\Delta M_z(\mathbf{r},t)$ can be approximately divided into the change in the longitudinal and transverse components of magnetization,

$$\Delta M_z(\mathbf{r},t) \simeq \tilde{m}_Z(\mathbf{r},t)\cos\theta_M - \tilde{m}_Y(\mathbf{r},t)\sin\theta_M. \qquad \text{(A3)}$$

The first term comes from the change in the longitudinal component, namely the change in the magnetization magnitude dynamics. The second term stems from the change in the transverse component of magnetization, corresponding to the spin-wave dynamics. The X-Y-Z coordinate system is also found in Fig. 1 in the main text. Thus, using Eqs. (A1) and (A3), $\Delta\theta_K(\mathbf{r},t)$ can be expressed by the summation of the

terms:

$$\Delta\theta_K(\mathbf{r},t) \simeq \Delta\theta_K^{\mathrm{mag}}(\mathbf{r},t) + \Delta\theta_K^{\mathrm{sw}}(\mathbf{r},t), \tag{A4}$$

$$\Delta\theta_K^{\mathrm{mag}}(\mathbf{r},t) = \frac{\theta_{K,S}}{M_S}\cos\theta_M \iint \tilde{m}_Z(\mathbf{r}-\mathbf{r}',t) g_p(\mathbf{r}') d^2r', \tag{A5}$$

$$\Delta\theta_K^{\mathrm{sw}}(\mathbf{r},t) = -\frac{\theta_{K,S}}{M_S}\sin\theta_M \iint \tilde{m}_Y(\mathbf{r}-\mathbf{r}',t) g_p(\mathbf{r}') d^2r'. \tag{A6}$$

2. Demagnetization

In this section, we derive the analytical expression from Eq. (A5) for use in the data analysis for the experimental data. In Eq. (A5), $\tilde{m}_Z(\mathbf{r},t)$ is expressed as

$$\tilde{m}_Z(\mathbf{r},t) \simeq \delta M(\mathbf{r}) + \delta\tilde{M}(\mathbf{r},t). \tag{A7}$$

The first term describes the time-averaged change of $|\mathbf{M}|$ due to the average temperature increase in the focal spot of the pump laser, which may be caused by heat accumulation during the period that the light chopper is on since the pulse repetition ($\simeq$10 ns) could be relatively shorter than the heat dissipation time. The second term corresponds to the temporal change of $|\mathbf{M}|$ in the picosecond time scale. Each term can further be expressed with the constant values of δM_0, δM_1, and δM_2 as follows:

$$\delta M(\mathbf{r}) = \delta M_0 G_m(\mathbf{r}), \tag{A8}$$

$$\delta\tilde{M}(\mathbf{r},t) = \left[\delta M_1 + \delta M_2 \exp\left(-\frac{t}{\tau}\right)\right]\Theta(t) G_m(\mathbf{r}). \tag{A9}$$

Here $\Theta(t)$ is the Heaviside's step function. The spatial profile of the demagnetization is assumed to be a Gaussian function $G_m(\mathbf{r})$ with time-independent width σ_m:

$$G_m(\mathbf{r}) = \exp\left(-\frac{r^2}{2\sigma_m^2}\right). \tag{A10}$$

This may imply that the heat dissipation in the film plane is slower than that into the substrate. Here we take only one time constant τ, characterizing the temporal recovery to equilibrium for magnetization, which is partially caused by nonequilibrium heat dissipation into the lattice system. We finally obtain the following relation for $t > 0$ using Eqs. (A5), (A7)–(A10):

$$\Delta\theta_K^{\mathrm{mag}}(\mathbf{r},t) = \frac{\theta_{K,S}}{M_S}\cos\theta_M G_{\mathrm{mp}}(\mathbf{r}) \times\left[\delta M_0 + \delta M_1 + \delta M_2 \exp\left(-\frac{t}{\tau}\right)\right], \tag{A11}$$

where the Gaussian function $G_{\mathrm{mp}}(\mathbf{r})$ is defined as:

$$G_{\mathrm{mp}}(\mathbf{r}) = \left(\frac{\sigma_m}{\sigma_{\mathrm{mp}}}\right)^2 \exp\left(-\frac{r^2}{2\sigma_{\mathrm{mp}}^2}\right), \tag{A12}$$

$$\sigma_{\mathrm{mp}} = \sqrt{\sigma_m^2 + \sigma_p^2}. \tag{A13}$$

This means that the observed Gaussian profile for $\Delta\theta_K^{\mathrm{mag}}$ in space becomes broader as a result of the finite probe beam spot size.

Note that the finite-time constant for ultrafast demagnetization was disregarded because it is much faster than the magnetization dynamics described here in conventional metals such as permalloys. We also disregarded any other ultrafast processes, such as superdiffusion spin current, which are outside the scope of this Appendix. More rigorous and detailed physical discussions can been found in other studies [25,49].

3. Spin wave

In this section, Eq. (7) is derived from Eq. (A6). The theory on MSWs has been intensively developed [50]. Here we consider the so-called thin-film limit; the Green function for the magnetostatic field generated from the spin wave is not considered [36]. The MSWs are theoretically expressed by the nonlocal space-time relationship between the transverse magnetization $\tilde{m}_Y$ and the transverse effective magnetic field $\tilde{h}_X$ and $\tilde{h}_Y$ induced by the pump laser pulse under a linear response regime:

$$\tilde{m}_Y(\mathbf{r},t) = \sum_{j=X,Y}\iiint \tilde{\chi}_{Yj}(\mathbf{r}-\mathbf{r}',t-t')\tilde{h}_j(\mathbf{r}',t') d^2r'dt', \tag{A14}$$

where $\tilde{\chi}_{Yj}$ is the radio-frequency magnetic susceptibility tensor. The physical variables in wave number $\mathbf{k} = (k_x,k_y)$ and angular frequency ω space are defined by the Fourier and inverse Fourier transforms:

$$\tilde{a}(\mathbf{k},\omega) = \iiint \tilde{a}(\mathbf{r},t) e^{-i(\mathbf{k}\cdot\mathbf{r}+\omega t)} d^2r dt,$$

$$\tilde{a}(\mathbf{r},t) = \frac{1}{(2\pi)^3}\iiint \tilde{a}(\mathbf{k},\omega) e^{i(\mathbf{k}\cdot\mathbf{r}+\omega t)} d^2k d\omega.$$

The Fourier transform of Eq. (A14) yields:

$$\tilde{m}_Y(\mathbf{k},\omega) = \sum_{j=X,Y}\tilde{\chi}_{Yj}(\mathbf{k},\omega)\tilde{h}_j(\mathbf{k},\omega). \tag{A15}$$

Then, the following relation is obtained using Eqs. (A6), (A14), and (A15):

$$\Delta\theta_K^{\mathrm{sw}}(\mathbf{r},t) = -\frac{\theta_{K,S}}{M_S}\sin\theta_M \sum_{j=X,Y}\iiint d^2k d\omega \times \tilde{\chi}_{Yj}(\mathbf{k},\omega)\tilde{h}_j(\mathbf{k},\omega) g_p(\mathbf{k}) e^{i(\mathbf{k}\cdot\mathbf{r}+\omega t)}, \tag{A16}$$

where $g_p(\mathbf{k})$ is the Fourier transform of $g_p(\mathbf{r})$:

$$g_p(\mathbf{k}) = \exp\left(-\tfrac{1}{2}\sigma_p^2 k^2\right). \tag{A17}$$

The Fourier transform of the experimentally observed data $\Delta\theta_K^{\mathrm{sw}}(x,t)[\equiv\Delta\theta_K^{\mathrm{sw}}(x,y=0,t)]$ can be expressed as

$$\Delta\theta_K^{\mathrm{sw}}(k_x,\omega) = \iint \Delta\theta_K^{\mathrm{sw}}(x,t) e^{-i(k_x x+\omega t)} dx dt. \tag{A18}$$

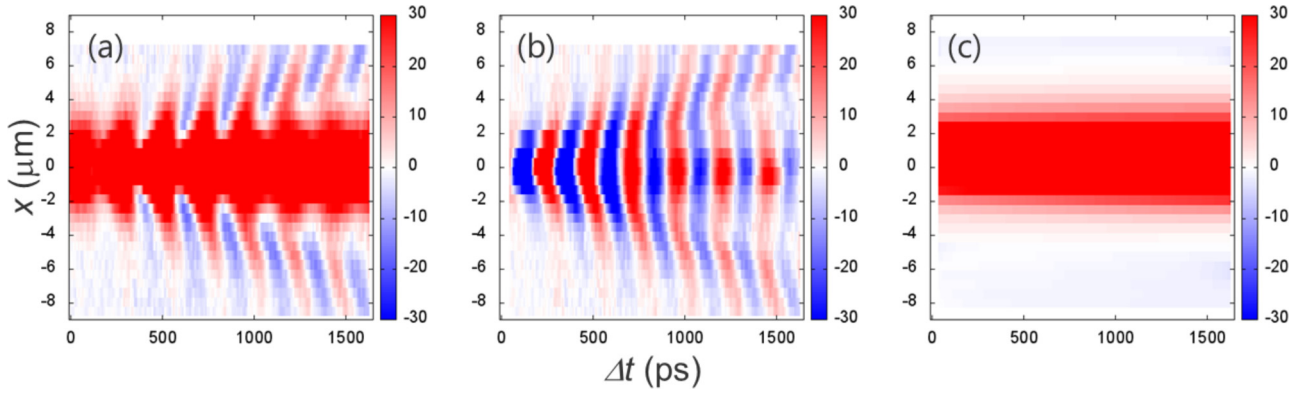

FIG. 8. The pump-laser-induced change in the Kerr rotation angle with different positions x and pump-probe delay times Δt: (a) uncorrected data $\Delta\theta_K(x,\Delta t)$ measured at $\theta_H = 4^\circ$. (b) after subtracting the demagnetization $\Delta\theta_K^{\rm sw}(x,\Delta t)$, and (c) the change in the Kerr rotation angle due to the demagnetization $\Delta\theta_K^{\rm mag}(x,\Delta t)$.

Substituting Eq. (A16) into Eq. (A18), the following general relationship between the observed data and $\tilde{\chi}_{Yj}$ is obtained:

$$\Delta\theta_K^{\rm sw}(k_x,\omega) = -\frac{\theta_{K,S}}{M_S}\sin\theta_M \sum_{j=X,Y}\int dk_y \times \tilde{\chi}_{Yj}(\mathbf{k},\omega)\tilde{h}_j(\mathbf{k},\omega)g_p(\mathbf{k}). \quad \text{(A19)}$$

Here we only consider $\tilde{h}_j$ due to the temporal change of the out-of-plane shape magnetic anisotropy by ultrafast demagnetization in the pump-focused area, which can be expressed as

$$\tilde{h}_j(\mathbf{r},t) = \delta\tilde{M}(\mathbf{r},t)\cos\theta_M \sin\theta_M \delta_{jY}. \quad \text{(A20)}$$

Its Fourier transform is given as follows:

$$\tilde{h}_Y(\mathbf{k},\omega) = \tilde{h}_Y(\omega)G_m(\mathbf{k})\delta_{jY}, \quad \text{(A21)}$$

$$\tilde{h}_Y(\omega) = \frac{1}{i\omega}\left(\delta M_1 + \frac{i\omega\tau}{1+i\omega\tau}\delta M_2\right) \times \cos\theta_M \sin\theta_M, \quad \text{(A22)}$$

where $G_m(\mathbf{k})$ is the Fourier transform of $G_m(\mathbf{r})$:

$$G_m(\mathbf{k}) = 2\pi\sigma_m^2 \exp\left(-\frac{1}{2}\sigma_m^2 k^2\right). \quad \text{(A23)}$$

By substituting Eqs. (A21)–(A23) into Eq. (A19), the following relation is obtained:

$$\Delta\theta_K^{\rm sw}(k_x,\omega) = \frac{\theta_{K,S}}{M_S}\tilde{h}_Y(\omega)G_{\rm mp}(k_x) \times \int \tilde{\chi}_{YY}(\mathbf{k},\omega)G_{\rm mp}(k_y)dk_y. \quad \text{(A24)}$$

Here

$$G_{\rm mp}(k_l) = \sqrt{2\pi}\sigma_m \exp\left(-\tfrac{1}{2}\sigma_{\rm mp}^2 k_l^2\right), \quad (l = x,y). \quad \text{(A25)}$$

Equations (A24) and (A25) are the main results in this section: The Fourier transform of the experimentally observed one-dimensional data contains the information of $\tilde{\chi}_{YY}$ averaged by the Gaussian function along the k_y axis.

For simplicity, we crudely approximate $\tilde{\chi}_{YY}(\mathbf{k},\omega)$ as

$$\tilde{\chi}_{YY}(\mathbf{k},\omega) \simeq \tilde{\chi}_{YY}(k_x,k_y=0,\omega) \quad \text{(A26)}$$

for k_y below $\sqrt{2}\sigma_{\rm mp}^{-1}$. Because the dispersion relation of MSSW with $k_y = 0$ is more dispersive than that of magnetostatic backward volume spin-wave (MSBVW) with $k_x = 0$, resulting in the heavily anisotropic dispersion relation of MSW in conventional magnetic metal films with a 10- to 100-nm-thickness range. Using the condition $\omega\tau \ll 1$ in Eq. (A22), we obtain the following proportionality from Eq. (A24):

$$\Delta\theta_K^{\rm sw}(k_x,\omega) \propto i\tilde{\chi}_{YY}(k_x,k_y=0,\omega)G_{\rm mp}(k_x). \quad \text{(A27)}$$

The $\tilde{\chi}_{YY}(\mathbf{k},\omega)$ can be generally approximated as the complex Lorentzian function with eigenfrequency $\omega_{\mathbf{k}}$ and its lifetime $\tau_{\mathbf{k}}$:

$$\tilde{\chi}_{YY}(\mathbf{k},\omega) \simeq \frac{\omega_M}{\omega - \omega_{\mathbf{k}} + i/\tau_{\mathbf{k}}}, \quad \text{(A28)}$$

where $\omega_M = \mu_0\gamma M_S$ and γ is the gyromagnetic ratio. In Eq. (A28), we assumed $\omega \simeq \omega_{\mathbf{k}}$ and that the Gilbert damping constant is much less than unity. Equations (A27) and (A28) show that the real (imaginary) part of $\Delta\theta_K^{\rm sw}(k_x,\omega)$ has an absorption (dispersion) curve with respect to ω, as described in the main text.

APPENDIX B: DATA ANALYSIS

Figure 8(a) shows the pump-laser-induced change in the Kerr rotation angle $\Delta\theta_K$ with different positions x and pump-probe delay times Δt. The magnitude of $\Delta\theta_K$ is large near $x = 0$ μm, which is due to the demagnetization. It is much larger than the magnitude of $\Delta\theta_K$ stemming from MSSW. To investigate $\Delta\theta_K$ stemming from MSSW, we approximately separate it from $\Delta\theta_K$ according to Eq. (A4):

$$\Delta\theta_K(x,\Delta t) \simeq \Delta\theta_K^{\rm mag}(x,\Delta t) + \Delta\theta_K^{\rm sw}(x,\Delta t), \quad \text{(B1)}$$

where the first and second terms on the right-hand side of the equation represent $\Delta\theta_K$ due to the demagnetization and MSSW, respectively. Subsequently, part of $\Delta\theta_K^{\rm mag}$ was treated as background and subtracted from the collected original data at each x using the following relation:

$$\Delta\theta_K^{\rm mag}(\Delta t) = A + Be^{-\Delta t/\tau}, \quad \text{(B2)}$$

where A and B are constant and τ is a time constant determined by the fitting to the experimental data of $\Delta\theta_K$ with respect to

Δt at each position x. Equation (B2) approximates Eq. (A11) in such a way that the spatial dependencies of A, B, and τ can be determined by fitting to the experimental data. Figure 8(b) shows the data with the subtracted background, namely $\Delta\theta_K^{\mathrm{sw}}$, which is identical to Fig. 3(a). Figure 8(c) displays the data of $\Delta\theta_K^{\mathrm{mag}}$, which was calculated by using Eq. (B2) with the A, B, and τ determined by the fitting. Note that $\Delta\theta_K^{\mathrm{mag}}$ approximately showed a Gaussian distribution, namely A and B have Gaussian distributions against x, and τ was $\simeq$30 ps and nearly independent of x within acceptable errors.

[1] S. Bandyopadhyay and M. Cahay, Nanotechnology **20**, 412001 (2009).

[2] V. V Kruglyak, S. O. Demokritov, and D. Grundler, J. Phys. D. Appl. Phys. **43**, 264001 (2010).

[3] B. Lenk, H. Ulrichs, F. Garbs, and M. Münzenberg, Phys. Rep. **507**, 107 (2011).

[4] A. A. Serga, A. V. Chumak, and B. Hillebrands, J. Phys. D. Appl. Phys. **43**, 264002 (2010).

[5] M. Jamali, J. H. Kwon, S. M. Seo, K. J. Lee, and H. Yang, Sci. Rep. **3**, 3160 (2013).

[6] J. Lan, W. Yu, R. Wu, and J. Xiao, Phys. Rev. X **5**, 041049 (2015).

[7] T. Schneider, A. A. Serga, T. Neumann, B. Hillebrands, and M. P. Kostylev, Phys. Rev. B **77**, 214411 (2008).

[8] V. E. Demidov, M. P. Kostylev, K. Rott, P. Krzysteczko, G. Reiss, and S. O. Demokritov, Appl. Phys. Lett. **95**, 112509 (2009).

[9] K. Sekiguchi, K. Yamada, S. M. Seo, K. J. Lee, D. Chiba, K. Kobayashi, and T. Ono, Appl. Phys. Lett. **97**, 022508 (2010).

[10] A. V. Chumac, A. A. Serga, and B. Hillebrands, Nat. Commun. **5**, 4700 (2014).

[11] N. Sato, K. Sekiguchi, and Y. Nozaki, Appl. Phys. Exp. **6**, 063001 (2013).

[12] M. Bailleul, D. Olligs, C. Fermon, and S. O. Demokritov, Europhys. Lett. **56**, 741 (2001).

[13] M. Covington, T. M. Crawford, and G. J. Parker, Phys. Rev. Lett. **89**, 237202 (2004).

[14] F. Ciubotaru, T. Devolder, M. Manfrini, C. Adelmann, and I. P. Radu, Appl. Phys. Lett. **109**, 12403 (2016).

[15] S. Tamaru, J. A. Bain, R. J. M. van de Veerdonk, T. M. Crawford, M. Covington, and M. H. Kryder, Phys. Rev. B **70**, 104416 (2004).

[16] K. Perzlmaier, G. Woltersdorf, and C. H. Back, Phys. Rev. B **77**, 054425 (2008).

[17] S. Tamaru, J. A. Bain, M. H. Kryder, and D. S. Ricketts, Phys. Rev. B **84**, 064437 (2011).

[18] S. Bonetti, R. Kukreja, Z. Chen, F. Maciá, J. M. Hernández, A. Eklund, D. Backes, J. Frisch, J. Katine, G. Malm, S. Urazhdin, A. D. Kent, J. Stöhr, H. Ohldag, and H. A. Dürr, Nat. Commun. **6**, 8889 (2015).

[19] M. Bauer, O. Buttner, S. O. Demokritov, B. Hillebrands, V. Grimalsky, Y. Rapoport, and A. N. Slavin, Phys. Rev. Lett. **81**, 3769 (1998).

[20] V. E. Demidov, S. Urazhdin, and S. O. Demokritov, Nat. Mater. **9**, 984 (2010).

[21] V. E. Demidov, S. Urazhdin, R. Liu, B. Divinskiy, A. Telegin, and S. O. Demokritov, Nat. Commun. **7**, 10446 (2016).

[22] A. A. Serga, T. Schneider, B. Hillebrands, S. O. Demokritov, and M. P. Kostylev, Appl. Phys. Lett. **89**, 63506 (2006).

[23] V. E. Demidov and S. O. Demokritov, IEEE Trans. Magn. **51**, 0800215 (2015).

[24] E. Beaurepaire, J.-C. Merle, A. Daunois, and J.-Y. Bigot, Phys. Rev. Lett. **76**, 4250 (1996).

[25] M. Battiato, K. Carva, and P. M. Oppeneer, Phys. Rev. Lett. **105**, 027203 (2010).

[26] M. van Kampen, C. Jozsa, J. T. Kohlhepp, P. LeClair, L. Lagae, W. J. M. de Jonge, and B. Koopmans, Phys. Rev. Lett. **88**, 227201 (2002).

[27] A. Barman, S. Wang, O. Hellwig, A. Berger, E. E. Fullerton, and H. Schmidt, J. Appl. Phys. **101**, 09D102 (2007).

[28] S. Mizukami, F. Wu, A. Sakuma, J. Walowski, D. Watanabe, T. Kubota, X. Zhang, H. Naganuma, M. Oogane, Y. Ando, and T. Miyazaki, Phys. Rev. Lett. **106**, 117201 (2011).

[29] J. Becker, O. Mosendz, D. Weller, A. Kirilyuk, J. C. Maan, P. C. M. Christianen, T. Rasing, and A. Kimel, Appl. Phys. Lett. **104**, 152412 (2014).

[30] S. Mizukami, A. Sugihara, S. Iihama, Y. Sasaki, K. Z. Suzuki, and T. Miyazaki, Appl. Phys. Lett. **108**, 12404 (2016).

[31] T. Satoh, Y. Terui, R. Moriya, B. A. Ivanov, K. Ando, E. Saito, T. Shimura, and K. Kuroda, Nat. Photon. **6**, 662 (2012).

[32] Y. Au, M. Dvornik, T. Davison, E. Ahmad, P. S. Keatley, A. Vansteenkiste, B. Van Waeyenberge, and V. V. Kruglyak, Phys. Rev. Lett. **110**, 097201 (2013).

[33] S. J. Yun, C. G. Cho, and S. B. Choe, Appl. Phys. Exp. **8**, 063009 (2015).

[34] S. Iihama, Y. Sasaki, A. Sugihara, A. Kamimaki, Y. Ando, and S. Mizukami, Phys. Rev. B **94**, 020401(R) (2016).

[35] Y. Sasaki, K. Suzuki, A. Sugihara, A. Kamimaki, S. Iihama, Y. Ando, and S. Mizukami, Appl. Phys. Express **10**, 23002 (2017).

[36] R. D. McMichael and P. Krivosik, IEEE Trans. Magn. **40**, 2 (2004).

[37] K. Di, V. L. Zhang, H. S. Lim, S. C. Ng, M. H. Kuok, J. Yu, J. Yoon, X. Qiu, and H. Yang, Phys. Rev. Lett. **114**, 047201 (2015).

[38] H. T. Nembach, J. M. Shaw, M. Weiler, E. Ju, and T. J. Silva, Nat. Phys. **11**, 825 (2015).

[39] A. A. Stashkevich, M. Belmeguenai, Y. Roussignè, S. M. Cherif, M. Kostylev, M. Gabor, D. Lacour, C. Tiusan, and M. Hehn, Phys. Rev. B **91**, 214409 (2015).

[40] M. Belmeguenai, J.-P. Adam, Y. Roussigne, S. Eimer, T. Devolder, J.-V. Kim, S. M. Cherif, A. Stashkevich, and A. Thiaville, Phys. Rev. B **91**, 180405 (2015).

[41] H. S. Korner, J. Stigloher, H. G. Bauer, H. Hata, T. Taniguchi, T. Moriyama, T. Ono, and C. H. Back, Phys. Rev. B **92**, 220413 (2015).

[42] O. Gladii, M. Haidar, Y. Henry, M. Kostylev, and M. Bailleul, Phys. Rev. B **93**, 054430 (2016).

[43] T. Sebastian, K. Schultheiss, B. Obry, B. Hillebrands, and H. Schultheiss, Front. Phys. **3**, 1 (2015).

[44] K. Nawaoka, Y. Shiota, S. Miwa, H. Tomita, E. Tamura, N. Mizuochi, T. Shinjo, and Y. Suzuki, J. Appl. Phys. **117**, 17A905 (2015).

[45] K. Nawaoka, S. Miwa, Y. Shiota, N. Mizuochi, and Y. Suzuki, Appl. Phys. Express **8**, 063004 (2015).

[46] The penetration depth for the light intensity is equal to $\lambda/4\pi\kappa$ with light wavelength λ and the imaginary part of the refractive index κ. It may be estimated to be about 14 (12) nm for the probe (pump) laser in this study, when κ for $Ni_{81}Fe_{19}$ of 4.43 (2.73) at $\lambda = 809$ (405) nm was used [47,48].

[47] T. M. Crawford, C. T. Rogers, T. J. Silva, and Y. K. Kim, Appl. Phys. Lett. **68**, 1573 (1996).

[48] C. L. Foiles, in *Landolt-Bornstein: Numerical Data and Functional Relationships in Science and Technology*, edited by K. H. H. E. Madelung (Springer, Berlin, 1985), Vol. 15b, p. 443.

[49] F. Dalla Longa, J. T. Kohlhepp, W. J. M. de Jonge, and B. Koopmans, Phys. Rev. B **75**, 224431 (2007).

[50] B. A. Kalinikos and A. N. Slavin, J. Phys. C **19**, 7013 (1986).